Three-Phase Flow Tomography System in Upward-Vertical High-Viscous-Oil/Water/Gas Flow

Hugo Fernando Velasco-Peña, *Senior Member, IEEE*, Adriana Bonilla-Riaño, Carlos Marlon Santos, and Oscar M. H. Rodriguez

***Abstract*— A new three-phase flow tomography system is presented in this work. The system was developed to be applied in high-viscous-oil/water/gas flow arranged in different flow patterns, with the three fluids present simultaneously in a crossing point. The primary measurement is based on a simpler and reliable digital in-phase/quadrature (IQ) demodulator and a wire-mesh sensor (WMS), but the system is capable of including different types of primary measurements. Dynamic three-phase flow tests were carried out to verify the system performance and compare its results with the ones obtained by quick-closing valves (QCVs) and a high-speed video camera. *In situ* volumetric fractions and flow patterns were compared. The experiments were conducted in a vertical glass pipe of 50-mm i.d. and 12-m height. The observed three-phase flow patterns were water-continuous churn flow with dispersed bubbles and oil drops (WChBoDo), water-continuous slug flow with Taylor bubbles, spherical bubbles, and oil drops (WPiBoDo), and oil-continuous slug flow with Taylor bubbles, spherical bubbles, and water drops (OPiBoDi). Compared with the measurements using QCVs, the average relative errors of the measured volumetric phase fractions were 12% for water, 13% for air, and 22% for oil. The experimental results, including the details of the flow inside the pipe, the phase distributions, and the objective characterization of flow patterns, suggest that the proposed system is a promising option for three-phase flow-related studies and developments. The proposed technique can reach 8930 frames/s with a 16 × 16 WMS.**

***Index Terms*— Flow patterns, impedance measurement, three-phase flow, tomography, wire-mesh.**

I. Introduction

OIL–WATER–GAS flow is frequently found in the energy industry. For instance, in the production stage, gas and oil reservoirs can include water naturally in wells, risers, or pipelines. In addition, some artificial lift techniques apply gas or water injection to enhance the production of heavy oils. Finally, thermodynamic alterations of the flow properties, especially due to decompression and heat transfer, can result in the hydrocarbons' phase change from liquid to a gaseous state. Therefore, the study of three-phase flow is essential to optimize oil and gas recovery and transport. This is even more important considering the current world production scenario, where unconventional oil is becoming more and more attractive [1].

Hence, by Huang *et al.* [2], experiments were carried out to obtain three-phase flow pattern maps in hilly terrain. Additionally, the authors studied flow-pattern transitions, pressure drop, and methods for the extraction and transport of heavy oil. Hanafizadeh *et al.* [3] determined flow patterns of air–water–oil flow in pipes with different inclinations. This classification was made by visual inspection of images taken laterally. Gawas [4] studied the entrainment of water and oil droplets in a dominant gaseous phase. In [5], the three-phase pressure drop is compared with the two-phase pressure drop in similar flow patterns. Liu *et al.* [6] proposed a new method to calculate the frictional pressure gradient in vertical flows. Three-phase flow patterns were identified via conductance signals by Xie *et al.* [7], where the features of the oil–gas–water flow signals were obtained by multiscale analysis method, and a parameter was proposed to identify the current flow pattern in the pipe. Al-Hadhrami *et al.* [8] studied the effect of water cut, liquid, and gas velocities on flow patterns and pressure gradients in horizontal pipes, offering detailed flow maps. Oddie *et al.* [9] presented flow-pattern and pressure-gradient data as well, but at different inclinations, and studied transient flows. In most of these works only basic and global variables, such as pressure drop, volumetric fraction, or the water layer height were measured. Also, frequently the authors show lateral images of the flow patterns obtained by high-speed cameras (HSCs). Remarkably, these images are complemented by the author's hand-made plots of the phases' distribution. Moreover, those types of plots were used to represent the longitudinal or cross-sectional distributions and no quantitative results were obtained. Zhao *et al.* [10] proposed a method based on microwaves, time series, and neural networks to predict the water-to-liquid ratio. It is clear from the literature review that in recent years there is a renewed interest in the study of three-phase flow [11], [12]. Therefore, the review of Yacub *et al.* [11], about gas–oil–water experiments, shows six (between 80 works) including viscous oil in their title, reaching up to 300 mPa·s. In this section, the reviewers mention seven

Manuscript received October 9, 2021; revised January 18, 2022; accepted February 14, 2022. Date of publication March 4, 2022; date of current version March 22, 2022. This work was supported in part by PETROBRAS through the project "Comparação entre Métodos de Elevação Artificial para Óleos Viscosos com Gás" under Grant 0050.0082074.13.9 and in part by CNPq "Bolsa de produtividade" under Grant 311057/2020-9. The Associate Editor coordinating the review process was Yixin Ma. *(Corresponding author: Hugo Fernando Velasco-Peña.)*

Hugo Fernando Velasco-Peña is with the Electrical Engineering Program, Universidad de La Salle, Bogotá 111711, Colombia (e-mail: hvelasco@lasalle.edu.co).

Adriana Bonilla-Riaño is with the Engineering School, Universidad de La Salle, Bogotá 111711, Colombia (e-mail: abonillar@gmail.com).

Carlos Marlon Santos is with the Industrial Multiphase Flow Laboratory, University of São Paulo, São Paulo 13566-590, Brazil (e-mail: carlosmarlon@alumni.usp.br).

Oscar M. H. Rodriguez is with the Mechanical Engineering Department, University of São Paulo, São Paulo 13566-590, Brazil (e-mail: oscarmhr@sc.usp.br).

Digital Object Identifier 10.1109/TIM.2022.3156990

works with their viscosity: six with viscosities between 1.2 and 11.98 mPa·s, and only one with 102 mPa·s. This shows that there are few experiments with viscous oil.

Until now, the work on three-phase flows with wire-mesh sensors uses flow patterns with restrictions that simplified the problem. For instance, in [13] and [14], they used stratified patterns, so at each crossing point, there was only a two-phase problem. Other works are limited to low oil volumetric fraction [15]. There are three laboratories using oil: multiphase flow laboratory (Nottingham University), which uses silicone oil with a viscosity of 5.3 mPa·s [14]; multiphase flow laboratory (Tianjin University), which uses oil with a viscosity of 3.5 mPa·s [15]; and thermal-fluids engineering laboratory (University of Sao Paulo), which uses oil with a viscosity up to 204 mPa·s [16] (this work used the last laboratory). According to the literature review, only one laboratory performs experiments with viscous oil and wire-mesh sensor (WMS).

A. Tomographic Flow Imaging

A tomographic image is a 2-D representation of a slice through an object. This kind of representation of flow-through imaging has been used for multiphase flow studies in many works [17]–[19]. Particularly, some authors have developed specialized systems for the three-phase flow case. Frøystein *et al.* [20] developed a dual-energy gamma-ray tomography system applied on simulated static three-phase flows. That system could deliver a low-contrast image every 2 s. Schug and Arlt [21] used a fast X-ray computed tomography to obtain the image of a two-phase flow in structured packings. Appel *et al.* [22] used magnetic resonance (MR) to measure the velocity and phase fractions. However, those authors did not present the obtained tomographic images. Alfareh *et al.* [23] studied theoretically an ultrasonic sensor array using the finite element method for the case of three-phase distributions (in static experiments). Their results were promising, but they need to be verified experimentally. Electrical capacitance tomography (ECT) has been used in annular three-phase flows by Li *et al.* [24]. The authors used ECT to obtain images, the water–liquid ratio, and the liquid ratio. Wang *et al.* [25] designed an electrical resistance tomography (ERT)/ECT system to measure simultaneously the resistance and the capacitance, but it was only tested with simulated two-phase flows. Sun and Yang [26] presented a dual ERT/ECT for getting tomographic images in stratified oil–water–air distributions, but the system was not tested with the phases flowing. Another ERT/ECT system was used to visualize oil–water–air flows. Wang *et al.* [27] could establish the water and oil ratios, and the ERT/ECT gave better results than optical methods or ERT or ECT, used separately, to measure the mean concentration of the phases. However, Hernandez-Alvarado *et al.* [28] indicate that ERT is the least reliable method among wire-mesh tomography (WMT), optical void probe, and pressure transducers, with gamma densitometry as a reference, because it can under-predict local void fraction up to 40% and area average fractions up to 60%, depending on the conditions of the experiment. For the case of techniques with ionizing radiation, such as gamma-ray tomography, thenstalllation is expensive and demanding due to safety requirements instituted to prevent health risks. The current techniques based on MR have a low temporal resolution, which is a severe disadvantage when studying transient flows. The ERT/ECT techniques overcome the cited disadvantage, but give low-resolution images, requiring back-propagation algorithms to reconstruct the image, and have limitations depending on the type of flow pattern.

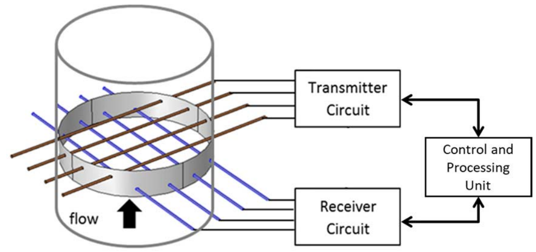

Fig. 1. Schematic representation of the wire-mesh sensor, with its location in a pipe.

On the other hand, the technique called WMT has been applied to multiphase flows successfully, in different applications and geometries, at a low cost. Several studies have compared WMT with other techniques. Dave *et al.* [29] summarize the comparisons, showing how this technique, despite being intrusive, can obtain the flow structure (compared to cameras), has good agreement with void fractions and gas velocity profile. (compared to X-ray tomography and gamma densitometry) and the interfacial area density measurements have good agreement (with a maximum deviation of 12% compared to needle probes). Also, Hernandez-Alvarado *et al.* [28] find that WMT gives differences of up to 5% for the local void fraction and area average void fractions, compared with gamma densitometry. In this work, we developed and implemented a WMT to work with high-viscous-oil/water/air flows.

A typical wire-mesh sensor is formed by two separated planes of wires. One plane has the transmitters and the other the receivers. The wires of each plane are positioned perpendicularly to the other plane, thereby forming a mesh of electrodes. In three-phase flow, each electrode or crossing point between wires measures the complex permittivity of the fluid's mixture, which is equivalent to measuring the electrical resistance and capacitance, simultaneously. In Fig. 1, the schematic of a 4×4 prototype can be observed. The spaces between the electrodes, at the crossing points, are filled with a mixture of fluids. Each transmitter wire (red) is activated in sequence and sends an electrical signal through the fluid. So, each receiver wire (blue) carries a signal containing the information to identify the characteristics of the fluids present at each crossing point. Nonactive transmitters are grounded. When the last transmitter wire has been activated, a full dataset of the type of fluid or phase fractions over the entire cross section is obtained. From this information, it is possible to obtain local mean fractions across the pipe's cross section, time, phase distributions along the section, *in situ* volumetric fraction, and 3-D images of the flow.

The WMT was first described by Johnson [30] as a sensor for measuring the fraction of water in oil, based on fluid conductivity/resistance. Most of the applications focused on gas-liquid flows [31]. Da Silva *et al.* [32] developed a WMS based on the measuring of the permittivity/capacitance of the fluids, which expanded the range of substances that can be identified. An extensive review of this technology is found by Velasco Peña and Rodriguez [33]. Overall, the sensor is intrusive. It means that the sensor or part of it is located in the flow path affecting the measurement to some degree. Even so, the technique can deliver a tomographic image with a good benefit–cost ratio, compared to other tomographic techniques such as X- or γ-rays.

The first attempt to use the wire-mesh sensor in oil–water–air flow was presented by da Silva [34]. He applied the capacitive wire mesh in a confined stratified system. Even though the three-phase system could be agitated, after some time the gravitational stratification of the phases assured that each measuring point would only discriminate between two phases. Therefore, the technique was limited to stratified flow patterns. Differently, in other works, two independent variables were measured; for instance: dos Santos *et al.* [35] and dos Santos [36] measured the changes of amplitude and the phase shift of a single-frequency sinusoidal signal. The authors showed the measurements in two different figures, without establishing any relation with the fraction of each phase. Due to the electrical circuits used, it was necessary to use two analog-to-digital converter (ADC) by each receiver wire. dos Santos *et al.* [13] applied two frequencies simultaneously, one of a relatively low frequency (75 kHz) and another of high frequency (1.825 MHz), to measure the conductivity and the permittivity, respectively. The phase fraction was determined by the mean of the Maxwell–Garnett permittivity relation. The system reached 781 frames/s with an 8 × 8 sensor. In both works, the sensor results were validated through tests carried out in small confined systems. They filled up a pipe segment with fluids, forming a stratified pattern, and simulated a flow by agitating the system.

In this work, we contribute to the development of the WMT technology by proposing a high-speed system to measure simultaneously both the conductivity and the permittivity of a mixture of three fluids. Dynamic flow tests in a large-scale multiphase-flow loop were carried out for that purpose. The proposed WMT applies a single-frequency sinusoidal signal to the fluid mixture and the measurement is done by IQ demodulator. The generator and the ADC's of the system are synchronized which allows a full-digital implementation of the demodulator. In addition, the processing system proposed in the present work is simpler and was implemented using the digital approach which means it has fewer analog circuits than those within other similar works [14].

II. Material and Methods

A. Experimental Setup

The experiments reported in this article were performed in the vertical loop of the Industrial Multiphase Flow Laboratory (LEMI) of the São Carlos School of Engineering, University of São Paulo, Brazil. The test section consisted of a glass line of 50 mm i.d. and 12 m in length. A bypass line allowed the use of the quick-closing-valve (QCV) technique to measure the *in situ* volumetric fraction of the phases. The tested liquid fluids, water, and high viscous oil (860 kg/m3 of density and 100 mPa·s of viscosity) were kept in polyethylene tanks. The air was stored in a pressurized tank. A compressor filled the air tank. Positive displacement water and oil pumps, both controlled by their respective variable-frequency drivers and pumped the phases to the test line. The airflow was controlled by electromechanical valves. Oil, water, and air were mixed at ground level at the beginning of the test section. Positive displacement and vortex flow meters were used to measure the flow rates of the fluids (see Table I).

TABLE I

Flowmeter Instrumentation on the Experimental Apparatus

Flowmeter	Measuring principle	Application	Flow range (l/min)	Uncertain (% do FS)
Badgermeter® OGT HF1/2"	Gear	Water flowmeter	1.00 – 35.00	±0.75
TechMeter TCM37BBEA10R	Turbine	Water flowmeter	31.60 - 333.40	±1.0
Oval® Ex – Delta	Gear	Water flowmeter	16.60 -1667.00	± 1.0
Oval M-III LSF45-L	Gear	Oil flowmeter	0.05 – 8.00	± 1.0
Oval® Flowpet LS5376-430A EG	Gear	Oil flowmeter	2.50 -106.70	± 1.0
Oval® Flowpet LS5576-430A EG	Gear	Oil flowmeter	6.67 – 233.40	± 1.0
Oval Gal – 50	Gear	Air flowmeter	4.00 – 20.00	± 1.0
Contech®- G9	Turbine	Air flowmeter	14.17 – 141 - 70	± 1.0
Contech®- G25	Turbine	Air flowmeter	141.70 – 1417.0	± 1.0
Contech®- G50	Turbine	Air flowmeter	566.8 - 5667.8	± 1.0

TABLE II

Experimental Uncertainties

Parameter	Uncertainty
Test section length	±5 mm
j_w	±1.0%
j_o	±0.5%
j_a	±1.3%
$\alpha_{a,QCV}$	±3,9%
$\alpha_{o,QCV}$	±3,0%
$\alpha_{w,QCV}$	±1,0%

TABLE III

Fluids' Electrical Properties

Fluid	Conductivity [S/m] σ	Relative Permittivity [.] ε
Air	1×10^{-15}	1.00
Oil	40×10^{-12}	3.5
Water	5×10^{-3}	80

The uncertainty analysis was made based on the accuracy of each equipment and uncertainty propagation theory. In Table II, the experimental uncertainties of the main parameters of this work are detailed.

After the test section, the liquids were separated from the air. Next, the oil–water mixture flowed to a coalescent-plate liquids separator tank, where gravitational separation of the two liquids was assured. Once separated, oil and water were returned to their respective tanks by gravity. The fluids' electrical features are presented in Table III.

B. Measurement System

The block diagram of the proposed measurement system is shown in Fig. 2. The measurement system heart consists of a signal generator and a data acquisition system based on an FPGA FlexRIO platform from National Instruments. The control is made by an FPGA board that synchronizes the

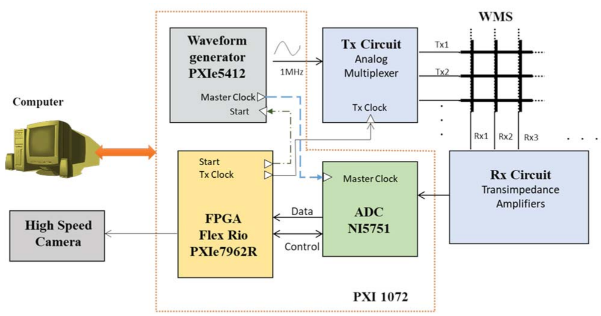

Fig. 2. Block diagram of the proposed measurement system.

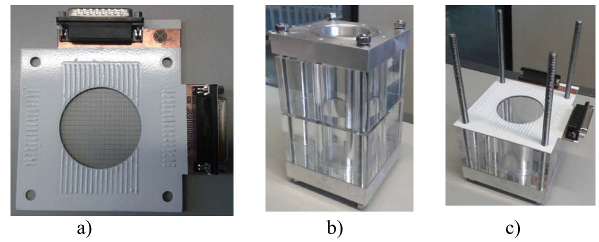

Fig. 3. (a) Homemade wire-mesh sensor (16 × 16 wires). (b) Acrylic box. (c) Wire-mesh sensor placed in between the two halves of the acrylic box.

operation between the generator, the data acquisition board, and the HSC.

The excitation signal (sine wave @ 1 MHz) is generated using an arbitrary signal generator PXIe-5412 and applied to the fluids through the transmitter (Tx) circuit, which is based on an analog multiplexer. Thus, this sinusoidal signal is applied to every transmitter wire (Tx1, Tx2, …, Tx16), one wire at one time. Once the entire set of transmitters has been activated, the measurement system gets one frame with the phase fraction data, as in the images in Fig. 9.

The sine wave is modified by the properties of the fluid and recovered by the receiver (Rx) circuit. It consists of transimpedance amplifiers. The analog-to-digital conversion is made using the ADC modules in the NI-5751 board. It has 16 acquisition channels with 50 MS/s each one, 14-bit resolution, the voltage range of $2V_{\mathrm{pp}}$, 50 Ω, and dc coupling. The receiver circuit has been specially designed to ensure compatibility with this board, as well as its protection. Finally, longitudinal images are taken using an HSC. An image is recorded at the same time as a frame of the measurement system.

The fluid properties are measured based on a proposed digital in-phase/quadrature (IQ) demodulator, based on the synchronization between the FPGA NI PXIe7962R, the signal generator NI PXIe-5412, and the ADC NI 5751, see details in Section II-D.

The settling time of all circuits (transmitter, WMS, and receiver) was not greater than 5.5 μs. For safety, the samples were only obtained after 6 μs. On the other hand, to obtain a measurement of the complex permittivity, it is necessary to obtain at least one full cycle of the excitation signal, which is 1 μs. Hence, the system can get a complete frame of the cross section sweeping the 16 transmitter wires, this corresponds to $16 \times (6 + 1)\ \mu\mathrm{s} = 112\ \mu\mathrm{s}$ or 8930 frames/s. It enables the system to be used to study transient flow phenomena and/or systems with very fast changes.

The implemented technique can generate approximately 243 MB/s and store around 17 min, in a 256-GB solid-state drive (SSD). The system can support transfer rates up to 950 MB/s, a limitation created by the maximum rate that supported the PXIe-7962R board. Several PXIe-7962R boards could be used to expand the system, to reach up to 3.2 GB/s, which is the maximum rate supported by the link to the PC (the communication board PCIe-PXIe-8381). The PC has a controller based on the Intel X79 architecture. This allows for supporting the theoretical maximum transfer rate directly to the RAM, achieving storage up to 56 GB of data, which equates to 59 s of experimental data. Although the implemented technique underuses the capacity of the system, it is possible to reach higher rates; especially if the settling time is improved. Besides, the flexibility of the designed system allows it to be adapted to other measurement techniques or the number of crossing points of the sensors can be expanded.

A homemade wire-mesh sensor was used to obtain the phase-fraction distributions and cross-sectional images of the flow [see Fig. 3(a)]. The sensor consisted of two cross-sectional planes made of 16 stainless steel wires of 0.1-mm diameter, the planes are separated by 1.4 mm, and there is 3 mm of distance between wires in the same plane. The design of the sensor obeys restrictions for its construction and sensitivity analysis made by da Silva [34], Prasser and Häfeli [37], and Zhang *et al.* [38]. Hence, the diameter of the wires (0.1 mm) was chosen in such a way that it would provide the least intrusiveness, but keep the wire stretched with the used welding method. Also, from an electrical point of view, the diameter has little effect on the sensitivity of each crossing point. The distance between planes must be as short as possible, in such a way that each crossing point is only sensitive to the electrical characteristics around it, avoiding crosstalk with neighboring points, so this distance is imposed by the plate on which the sensor was manufactured (1.4 mm). The distance between wires must take into account that the highest possible spatial resolution is reached and that crosstalk is minimized. The first condition allows the flow structures to be reconstructed in more detail. The second condition leads to having a distance between wires at least two times the distance between planes, that is > 2.8 mm (3 mm was chosen). Sensor lifetime is estimated at 16 h of experiments. The sensor was installed at 10.3 m from the tube entrance, between the two halves of a perspex visualization section and the QCVs. A lateral view of the flow was recorded using an Olympus i-Speed 3.

In Fig. 3, one can see the acrylic box used for visualization purposes [see Fig. 3(b)], the wire-mesh sensor placed in between the two halves of the acrylic box [see Fig. 3(c)], and the system installed in the test section (see Fig. 4). The acrylic pieces make it possible to visualize the upstream and downstream flow. The aluminum sections allow the flange to be attached to the piping. The sensor was placed in the pipe at 5.5 m downstream of the injection nozzle and 1 m downstream of the start of the test section.

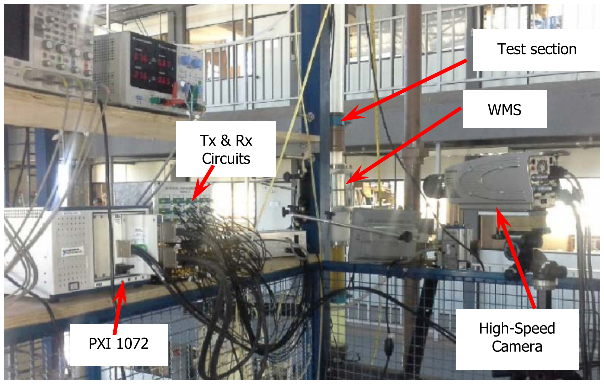

Fig. 4. Picture of the installed system in the test section.

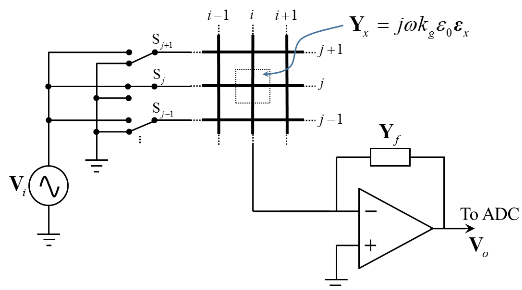

Fig. 5. General circuit diagram for measurement of complex permittivity using a wire-mesh sensor.

C. Measurement Principle

An inverting amplifier circuit is used to sense the electrical admittance of the fluid. Fig. 5 shows a general diagram of the implemented circuit. In Fig. 5, $\mathbf{Y}_f$ and $\mathbf{Y}_x$ are the feedback and fluid admittance, respectively, $\mathbf{V}_i$ is the excitation signal and $\mathbf{V}_o$ is the output signal. This circuit has a voltage gain defined by

$$\mathbf{A}_v = \frac{\mathbf{V}_o}{\mathbf{V}_i} = -\frac{\mathbf{Y}_x}{\mathbf{Y}_f}. \tag{1}$$

The electric current passing through the fluids at each crossing point travels by each receiver wire and arrives at the transimpedance amplifier. This amplifier has two essential features for the proper operation of the WMT technique. The first is that it is possible to adjust the input impedance to be significantly lower than the fluid impedance. The second is creating a virtual ground at the receiver wires. Thus, the currents that each amplifier receives are unambiguously related to the corresponding relative complex permittivity of the fluids $\boldsymbol{\varepsilon}_x$, at the crossing point. This can be expressed, for frequencies lower than 100‘s MHz, as

$$\boldsymbol{\varepsilon}_x = \varepsilon - \frac{j\sigma}{(\varepsilon_0\omega)} \tag{2}$$

where ε is the relative fluid permittivity or dielectric constant, σ is the fluid conductivity, ε_0 is the permittivity of free space and ω is the angular frequency. The relation between the fluid admittance $\mathbf{Y}_x$ and the complex fluid permittivity $\boldsymbol{\varepsilon}_x$ is given by

$$\mathbf{Y}_x = j\omega k_g \varepsilon_0 \boldsymbol{\varepsilon}_x \tag{3}$$

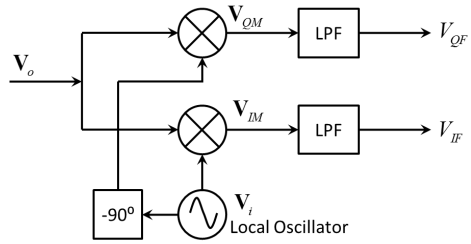

Fig. 6. Block diagram of an IQ demodulator.

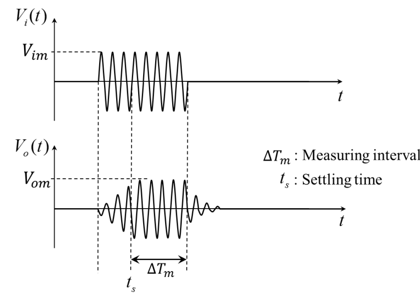

Fig. 7. Signals of excitation $V_i(t)$ and response $V_o(t)$ for the inverting amplifier circuit. The measure is done during the measuring interval ΔT_m.

where k_g is a constant related to the geometry of the sensor. Thus, the voltage gain is related to the complex fluid permittivity by

$$\mathbf{A}_v = -\frac{j\omega k_g \varepsilon_0 \boldsymbol{\varepsilon}_x}{\mathbf{Y}_f}. \tag{4}$$

In conclusion, in an ideal case, there is a proportional relation between $\mathbf{A}_v$ and $\boldsymbol{\varepsilon}_x$. In addition, knowing the voltage gain, it is possible to determine the complex fluid permittivity.

D. Measurement of the Fluid Admittance

The fluid admittance is measured through the IQ demodulator circuit, illustrated in Fig. 6. In this diagram, the response (output) signal of the inverting amplifier circuit $\mathbf{V}_o = V_{\text{om}}\cos(\omega_o t + \theta)$ is compared with the excitation signal $\mathbf{V}_i = V_{\text{im}}\cos(\omega_i t)$. The response of the circuit after each change of a transmitter wire looks similar to the one shown in Fig. 7. After a settling time (t_s), it is possible to compare the differences between amplitudes and phases to determine the fluid admittance.

In case that the two signals (excitation and response) have the same frequency, $\omega_i = \omega_o$, the outputs of the IQ demodulator are given by two constant dc voltages

$$V_{\text{IF}} = \frac{V_{\text{im}} V_{\text{om}} \cos(\theta)}{2} \tag{5}$$

$$V_{\text{QF}} = -\frac{V_{\text{im}} V_{\text{om}} \sin(\theta)}{2}. \tag{6}$$

Then, V_{om} and θ can be written as

$$V_{\text{om}} = 2 \cdot \sqrt{V_{\text{IF}}^2 - V_{\text{QF}}^2} / V_{\text{im}} \tag{7}$$

$$\theta = \tan^{-1}\left(-\frac{V_{\text{QF}}}{V_{\text{IF}}}\right). \tag{8}$$

The assumption that the two signals are the same is reasonable because the fluid admittance is considered linear and the time is considered invariable during the measuring time, ΔT_m. Thus, it is possible to recover the fluid admittance. The calibration process in Section II-E explains how to obtain this admittance.

In this methodology, the excitation signal is typically monitored using one of the available ADC channels. This implies having a channel less to the WMS and having a lower resolution or adding another ADC channel. Also, two ADC channels are typically used to sample the IQ signals by each receiver wire (Rx1, Rx2, ..., Rx16). To avoid this and to distinguish this system from other similar systems [13], a master clock signal synchronizes the excitation signal $\mathbf{V}_i$ generated by PXIe-5412 and the ADC sampling clock of NI-5751. The last has a phase-locked loop (PLL) that allows its perfect synchronization. Thus, with this strategy, only one ADC per receiver wire is necessary and special procedures to adjust the phase shift of the excitation signal are not necessary. The excitation signal can be reconstructed because the sampling instant is known. Moreover, if the number of samples per cycle (N_S) of the excitation signal is an integer, the low-pass filters (LPFs of the IQ demodulator) can be implemented as the mean of $k \cdot N_S$ sampled values, where k is an integer. This means that during the measuring interval an integer number of samples by cycle are taken. For an excitation frequency of 1 MHz the ADC obtain 50 samples by cycle, which allows reconstructing in detail the excitation and response signals. It simplifies the computational workload and designs a mostly digital system.

E. Calibration of the Complex Permittivity

The implemented circuit needs a calibration process to isolate the fluid admittance measurement of the residual admittance caused by parasitic resistances, the capacitances, inductance of the cables, temperature displacement, among others. Then, using the technique proposed by Da Silva *et al.* [39], the measured admittance $\mathbf{Y}_M$ at the crossing points can be described as

$$\mathbf{Y}_M = \mathbf{Y}_x + \mathbf{Y}_R \tag{9}$$

where, $\mathbf{Y}_R$ is the residual admittance. Thus, the real gain can be written as

$$\mathbf{A}_v = -\frac{\mathbf{Y}_M}{\mathbf{Y}_f} = -\frac{(\mathbf{Y}_x + \mathbf{Y}_R)}{\mathbf{Y}_f} \tag{10}$$

isolating $\mathbf{Y}_x$ is possible to see a linear relation with $\mathbf{A}_v$

$$\mathbf{Y}_x = -\mathbf{Y}_R - \mathbf{Y}_f \mathbf{A}_v \tag{11}$$

and equating with (3)

$$\mathbf{Y}_x = j\omega k_g \varepsilon_0 \boldsymbol{\varepsilon}_x = -\mathbf{Y}_R - \mathbf{A}_v \mathbf{Y}_f. \tag{12}$$

Thus, the complex permittivity can be obtained by

$$\boldsymbol{\varepsilon}_x = \varepsilon - \frac{j\sigma}{\omega\varepsilon_0} = \frac{\left(-\mathbf{Y}_R - \mathbf{Y}_f \mathbf{A}_v\right)}{j\omega k_g \varepsilon_0} = \boldsymbol{\mu} + \boldsymbol{\vartheta}\mathbf{A}_v \tag{13}$$

where $\boldsymbol{\mu}$ and $\boldsymbol{\vartheta}$ are complex constants. These constants are unique for each crossing point and can be calculated by calibration with two fluids of known complex permittivities $\boldsymbol{\varepsilon}_1$ and $\boldsymbol{\varepsilon}_2$. By using the fluid with permittivity $\boldsymbol{\varepsilon}_1$ a voltage gain $\mathbf{A}_{v1}$ will occur, and $\boldsymbol{\varepsilon}_2$ will produce $\mathbf{A}_{v2}$. Then, it is possible to write the constants as

$$\boldsymbol{\mu} = \frac{(\boldsymbol{\varepsilon}_2 \mathbf{A}_{v1} - \boldsymbol{\varepsilon}_1 \mathbf{A}_{v2})}{(\mathbf{A}_{v1} - \mathbf{A}_{v2})} \tag{14}$$

$$\boldsymbol{\vartheta} = \frac{(\boldsymbol{\varepsilon}_1 - \boldsymbol{\varepsilon}_2)}{(\mathbf{A}_{v1} - \mathbf{A}_{v2})}. \tag{15}$$

Thus, the relative fluid permittivity ε or dielectric constant and the fluid conductivity σ can be determined as

$$\varepsilon = \mathrm{Re}\{\boldsymbol{\mu} + \boldsymbol{\vartheta}\mathbf{A}_v\} = \mathrm{Re}\{\boldsymbol{\varepsilon}_x\} \tag{16}$$

$$\sigma = -\varepsilon_0\omega \mathrm{Im}\{\boldsymbol{\mu} + \boldsymbol{\vartheta}\mathbf{A}_v\} = -\varepsilon_0\omega \mathrm{Im}\{\boldsymbol{\varepsilon}_x\}. \tag{17}$$

The excitation frequency (1 MHz) was chosen so the system can be sensitive to the admittance variations (i.e., complex permittivity or conductivity and relative permittivity) related to the concentration of the used fluids. If the frequency were too low, the measurement system would be sensitive to the mixture conductivity changes but not to the relative permittivity changes. Similarly, if the frequency were too high, the system would detect the relative permittivity changes but not the conductivity variations [34]. In conclusion, the frequency should be between 100 kHz and 2 MHz. In this point, it is necessary additional research to determine the optimal frequency.

F. Three-Phase Relation Models

To find the correspondence between the measured complex permittivity $\boldsymbol{\varepsilon}_x$ and the local phase fractions α_i it is necessary to use a relation model, where α_i denotes the ith phase. There are few relation models for three-phase flows in the literature.

Table IV shows the relation models, parallel, series, Bruggeman, and homogeneous Maxwell–Garnett, for three-phase flows. The first two models were deducted for this study from the circuit theory, and Bruggeman and Maxwell–Garnett models were taken from [40]. Each one has a particular behavior. The parallel model is the only independent of the frequency. The Maxwell–Garnett model is the only non-self-consistent; this means that it is dependent on the continuous phase. Each model was designed for a specific electrode geometry and different distribution of the phases (flow pattern). In general, all the relation models shown in this article were developed for homogeneous electrical fields, which are not fully compatible

TABLE IV
THREE-PHASE RELATION MODELS

Model	Equation	
Parallel	$\boldsymbol{\varepsilon}_x = \boldsymbol{\varepsilon}_1(1-\alpha_2-\alpha_3) + \boldsymbol{\varepsilon}_2\alpha_2 + \boldsymbol{\varepsilon}_3\alpha_3$	(18)
Series	$\frac{\boldsymbol{\varepsilon}_1\boldsymbol{\varepsilon}_2\boldsymbol{\varepsilon}_3}{\boldsymbol{\varepsilon}_x} = \boldsymbol{\varepsilon}_2\boldsymbol{\varepsilon}_3 + \alpha_3\boldsymbol{\varepsilon}_3(\boldsymbol{\varepsilon}_1-\boldsymbol{\varepsilon}_2) + \alpha_3\boldsymbol{\varepsilon}_2(\boldsymbol{\varepsilon}_1-\boldsymbol{\varepsilon}_3)$	(19)
Bruggeman [38]	$0 = \alpha_1\frac{\boldsymbol{\varepsilon}_1-\boldsymbol{\varepsilon}_x}{\boldsymbol{\varepsilon}_1+2\boldsymbol{\varepsilon}_x} + \alpha_2\frac{\boldsymbol{\varepsilon}_2-\boldsymbol{\varepsilon}_x}{\boldsymbol{\varepsilon}_2+2\boldsymbol{\varepsilon}_x} + \alpha_3\frac{\boldsymbol{\varepsilon}_3-\boldsymbol{\varepsilon}_x}{\boldsymbol{\varepsilon}_3+2\boldsymbol{\varepsilon}_x}$	(20)
Maxwell-Garnett [38]	$\frac{\varepsilon_x-\varepsilon_1}{\varepsilon_x+2\varepsilon_1} = \alpha_2\frac{\varepsilon_2-\varepsilon_1}{\varepsilon_2+2\varepsilon_1} + \alpha_3\frac{\varepsilon_3-\varepsilon_1}{\varepsilon_3+2\varepsilon_1}$	(21)

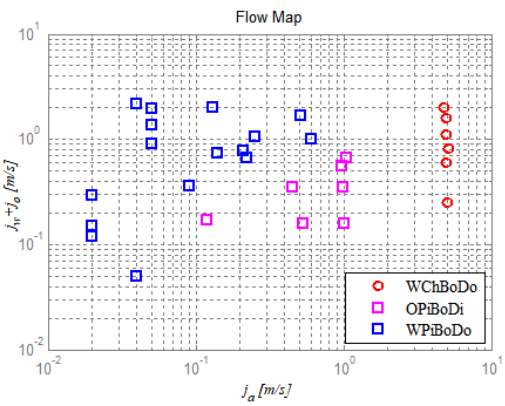

Fig. 8. Experimental flow-pattern map of the superficial velocities. The horizontal axis refers to the air superficial velocity, and the vertical axis refers to the liquids' mixture velocity.

with the conditions that exist at each crossing point of the wire-mesh sensor, since the electrodes are small compared with the flow structures.

It is possible to rewrite all these equations as a function of its phase fractions in the form

$$\mathbf{S} = \alpha_2 \mathbf{T} + \alpha_3 \mathbf{U} \tag{22}$$

where α_2 and α_3 are the phase fractions of the dispersed phases. Thus, using the continuity equation $\alpha_1 + \alpha_2 + \alpha_3 = 1$, the phase fractions are obtained by

$$\begin{bmatrix} \alpha_1 \\ \alpha_2 \\ \alpha_3 \end{bmatrix} = \begin{bmatrix} 0 & \mathrm{Re}(\mathbf{T}) & \mathrm{Re}(\mathbf{U}) \\ 0 & \mathrm{Im}(\mathbf{T}) & \mathrm{Im}(\mathbf{U}) \\ 1 & 1 & 1 \end{bmatrix}^{-1} \begin{bmatrix} \mathrm{Re}(\mathbf{S}) \\ \mathrm{Im}(\mathbf{S}) \\ 1 \end{bmatrix}. \tag{23}$$

In theory, it would be possible to improve the relative errors, the points spreading, and trends if a permittivity model was fit to a specific flow pattern. However, this does not guarantee that a permittivity model that is the best for predicting the water volumetric fraction for slug flow would be the best for another flow pattern or any other phase. In addition, this possible approach incorporates complexities and complications in the technique that would eventually reduce the applicability of using the wire-mesh sensor, since in field conditions it is not known, *a priori*, what the flow pattern is.

III. Experimental Results and Discussion

The proposed measurement system was used for measuring volumetric phase fractions in three-phase flow experiments and was compared with the QCV data. The ranges of superficial velocities were, gas: $j_a = 0.0 - 5.1$ m/s, water: $j_w = 0.0 - 1.5$ m/s, and oil: $j_o = 0.0$ and 1.85 m/s. The experimental flow map is presented in Fig. 8. The full set of experimental points is formed by 30 experiments.

A. Qualitative Results

The three-phase flow tomography by wire-mesh system offers access to inaccessible details of the flow by external observation, even using high-speed and high-resolution cameras. In Figs. 9–11, the tomographic images were taken at a rate of 1000 frames/s.

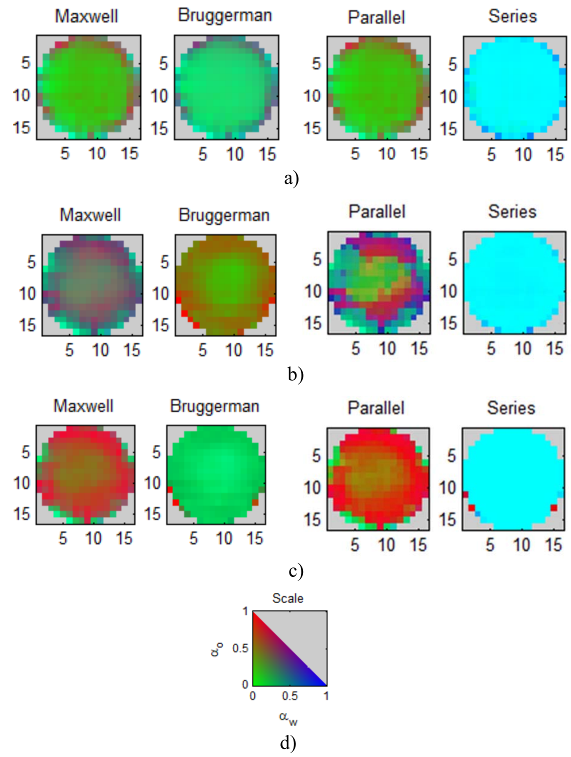

Fig. 9. Cross-sectional images (temporal mean) processed with Maxwell–Garnett; Bruggeman; parallel and series models. For (a) WChBoDo, (b) WPiBoDo and (c) OPiBoDi. (d) Color scale used to represent the fluids and their fractions; Water: blue; Oil: red; Gas: green.

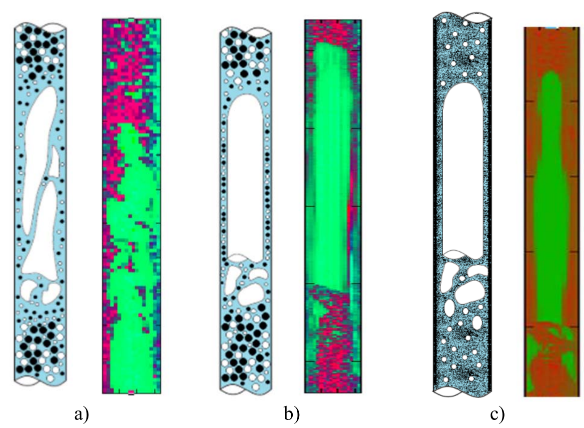

Fig. 10. Longitudinal tomography for each observed three-phase flow pattern, using Maxwell–Garnett model, where oil in water dispersion is represented by pink color, gas by green, and water in oil dispersion by brown. And graphical sketch for each observed three-phase flow pattern, where blue color represents water, white represents air, and black represents oil. The latter was taken from [43]. (a) WChBoDo. (b) WPiBoDo. (c) OPiBoDi.

The three-phase relation models, i.e., parallel, series, Bruggeman, and homogeneous Maxwell-Garnett; can be qualitatively compared. Fig. 9 presents the temporal mean of the water, the oil, and the air phase fractions of the transversal section, using those models, for each observed flow pattern. Phase fraction values are rational numbers. Each flow pattern has different characteristics; water-continuous churn flow with dispersed bubbles and oil drops (WChBoDo) has air in most

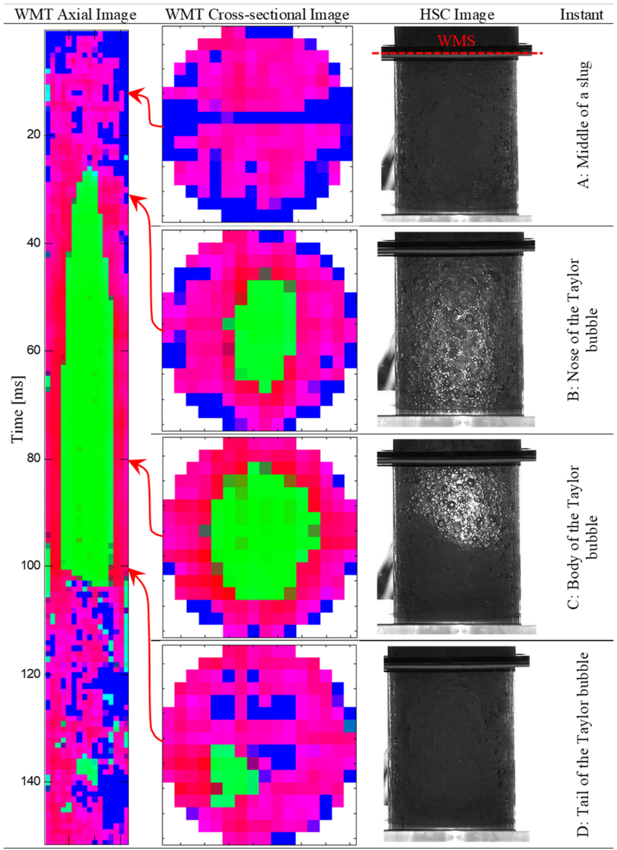

Fig. 11. Longitudinal (LHS) and cross-sectional images (middle) during the transit of a Taylor bubble in three-phase slug flow compared with the HSC ones (RHS). Image obtained at 1000 frames/s. Data were processed using the Maxwell–Garnett model. The color scale used is in Fig. 9(d).

of the pipe's cross section and oil–water mixture near to the pipe wall [see Fig. 9(a)]. In water-continuous slug flow with Taylor bubbles, spherical bubbles, and oil drops (WPiBoDo), one can observe the dominant water phase with dispersions of air and oil [see Fig. 9(b)]. In oil-continuous slug flow with Taylor bubbles, spherical bubbles, and water drops (OPiBoDi), there is a core of air with some water surrounded by an oil ring [see Fig. 9(c)].

B. Observed Flow Patterns

Three different three-phase flow patterns were observed, two dominated by water: water continuous flow (W) with churn flow (Ch), bubbles (Bo) and oil drops (Do), named as "WChBoDo," water continuous flow (W) with Taylor bubbles (Pi), spherical bubbles (Bo) and oil drops (Do), named as "WPiBoDo," and one where the dominant phase was oil: oil continuous flow (O) with Taylor bubbles (Pi), spherical bubbles (Bo) and dispersion of water drops in oil (Di), called "OPiBoDi." A longitudinal tomography from the pipe center of these three flow patterns is presented in Fig. 10, i.e., were used the crossing points measurements of transmitter 7 (Tx_7) and receivers 1–16 (Rx_1–Rx_{16}). The results are contrasted with graphical sketches because it was not possible to get a representative longitudinal tomography from the HSC. It is interesting pointing out some flow characteristics that are made visible from the WMS longitudinal images. For example, in Fig. 10(b) and (c), the dominant phases are water and oil, respectively, but the air's superficial velocity is almost the same. By inspection, it is clear that the Taylor bubble has a diameter near that of the pipe's when water is the dominant phase [see Fig. 10(b)], but when oil is dominant the liquid film is thicker [see Fig. 10(c)].

In Fig. 11, the results are for the test point with superficial velocities $j_o = 0.21$ m/s, $j_w = 0.66$ m/s, and $j_a = 0.12$ m/s and WPiBoDo flow pattern. In the middle, cross-sectional images corresponding to different instants of time are presented. By inspecting the longitudinal (LHS) and cross-sectional views (middle), one can see the typical shape of the Taylor bubble, whose nose presents a conical shape and rounded tip, and the tail is essentially cylindrical, occupying most of the tube diameter. At time A (less than 20 ms), the slug made of the liquid mixture is there, the image has blue and pink colors that correspond to water and oil, respectively, and water is the dominant phase that is in contact with the pipe wall. At the instant B (between 20 and 40 ms), the Taylor bubble begins; the bubble nose has an oval shape, and it is at the core of the pipe. The bubble is represented in green, denoting air, surrounded by an oil–water mixture. At time C (at 80 ms), halfway through the Taylor bubble body, the bubble becomes cylindrical. At instant D (at 100 ms), the end of the bubble, the tail is off the pipe center, and some dispersed air bubbles are present due to the turbulence. The images obtained by HSC confirm the main results but cannot be used to describe what is happening in the pipe's core. The results suggest that the oil concentration is greater near the bubble and the water concentration is greater near the wall. The color scale used to represent the fluids and their fractions can be seen at the bottom of Fig. 9(d): a water fraction equal to one (only water at the crossing point) is represented with the blue color, oil with red, and air with green. The intermediate colors were interpolated proportionally to the phase fraction. In the axial frames or 150 ms are illustrated. The longitudinal measurements were obtained with the central electrode.

These results have great value for the oil industry since the *in situ* properties of multiphase flow have a direct influence on the flow control and safety measures or for optimizing the production. Not to mention the possibilities of studying the average sizes of several flow structures as drops, cap bubbles, films near the pipe wall, among others.

In Fig. 12, one can see cross-sectional phase fractions as a function of time for each phase during 5-s time acquisition and in Fig. 13 the time lapse of transit of a Taylor bubble (0.15 s). In Fig. 12, one can observe the passage of 18 Taylor bubbles, denoted by the oscillations of the signals. The passage of a Taylor bubble is evidenced by a signal related to air (green).

In Fig. 13 one can see that the air fraction (green) strongly increases during the passage of a Taylor bubble. In most of the experiments, the system was robust and delivered reliable results that agreed qualitative and quantitatively to what was expected. However, the system is more sensitive when the oil and air phase fractions are high.

This is due to the similar values of the relative permittivity and the very low values of conductivity of these fluids.

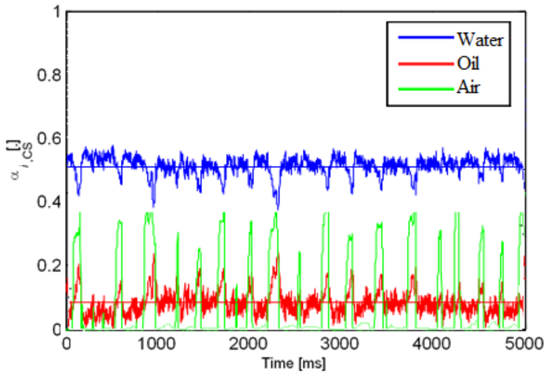

Fig. 12. Cross-sectional phase fractions as a function of time $(\alpha_{i,CS})$ during 5 s.

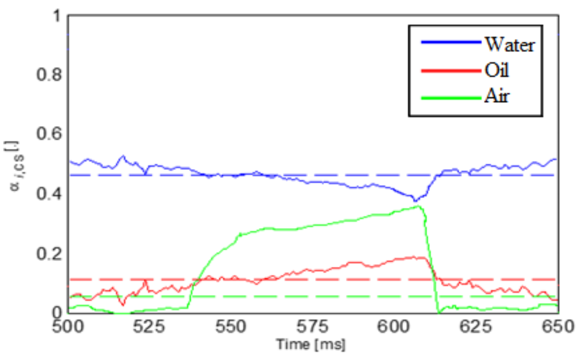

Fig. 13. Cross-sectional phase fractions as a function of time $(\alpha_{i,CS})$ during the transit of a Taylor bubble, 0.15 s.

The resolution of the system in those cases is relatively lower. Additionally, the natural noise of the system could produce deviations. When the noise is high, the phase-fraction values calculated by (23) can be negative, which have no physical meaning. In those special cases, the phase fraction is limited to zero, and the sum of the phase fractions reaches values a little higher than 1 (details about the wire-mesh data processing are described by Rodriguez *et al.* [41]).

C. Quantitative Results

The *in situ* volumetric fraction of the phases was obtained via the proposed tomography system for each experimental point, *ep*, and compared with the ones obtained using QCV (see Fig. 14). The average relative error (ARE) was used to quantify the comparison as follows:

$$\text{ARE}[\%] = 100\frac{\sum_{\exp=1}^{n}\sqrt{\left(\frac{\alpha_{\text{WMS,exp}}-\alpha_{\text{QCV,exp}}}{\alpha_{\text{QCV,exp}}}\right)^2}}{n}. \quad (24)$$

Inspecting Fig. 14, it is clear that the model that presents the smallest points spreading for all three volumetric fractions is the Maxwell–Garnett (21). It gave the smallest *ARE* for all volumetric fractions and flow patterns for the typical three-phase flows tested in this work (see Table V). The average relative error for water, air, and oil is 12%, 13%, and 22%, respectively.

The differences between the error of the volumetric fractions predicted by the models in Table V could be explained by

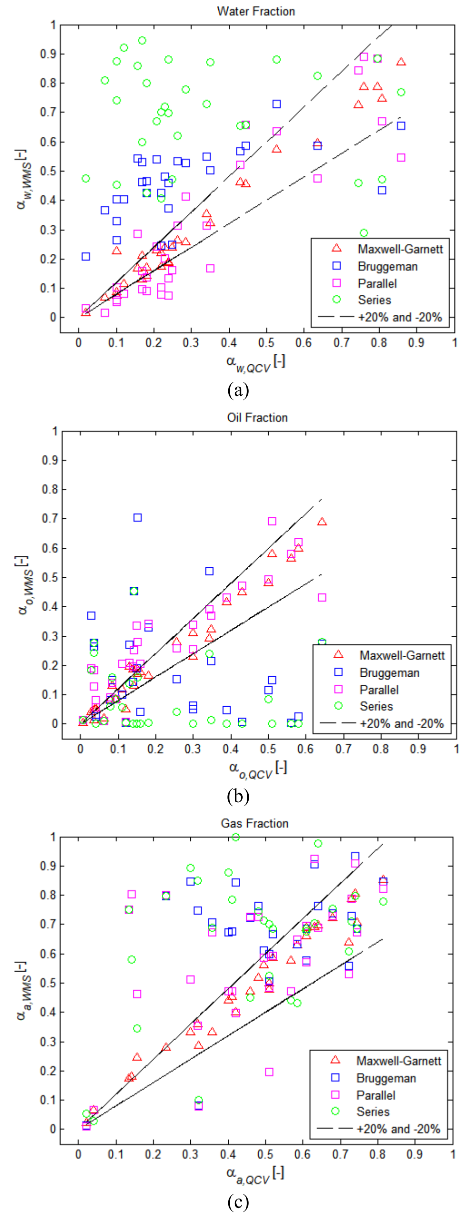

Fig. 14. Volumetric phase fractions measured by the proposed WMT compared with the ones measured by the QCVs using different relation models. (a) Water phase fraction. (b) Oil phase fraction. (c) Air phase fraction. The dashed lines indicate a deviation of ±20.

the conditions of the flows and the sensitivity of each model concerning each flow pattern. Each model was developed for a particular flow pattern, but in this study, the models were applied indiscriminately to all flow conditions tested and flow patterns to establish a suitable general model.

Qualitatively and quantitatively, the Maxwell–Garnett model had the best results for each studied flow pattern (see Fig. 9 and Table V). The Bruggeman model overestimates the air phase, and the series model overestimates the water phase. Restricting the analysis to the data obtained with the Maxwell–Garnett model only.

It is possible to observe in Fig. 15, that the WMS delivers the worst predictions for the lowest oil volumetric fractions. A likely reason for that is the fact that the oil electrical

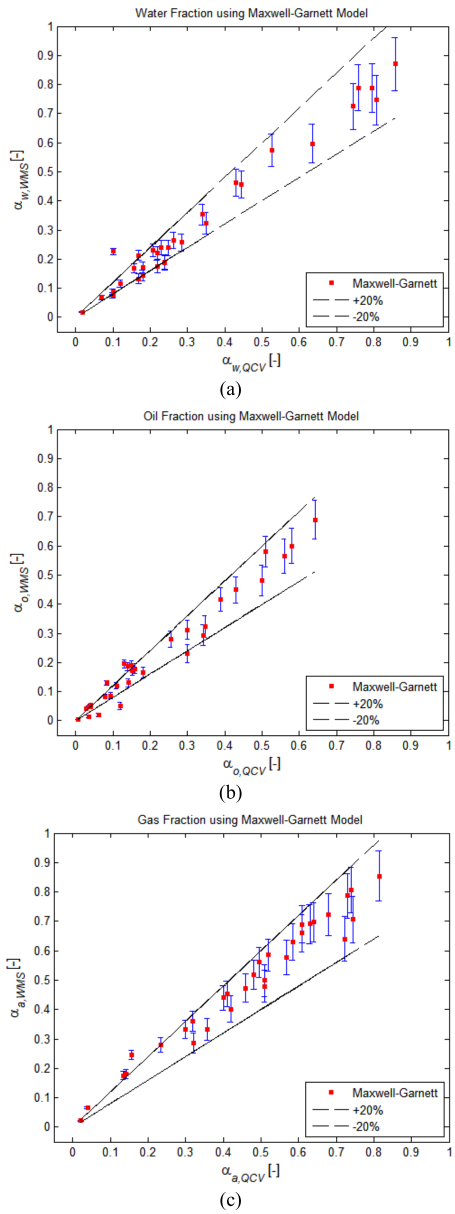

Fig. 15. Volumetric phase fractions measured by the proposed WMT compared with the ones measured by the QCVs using Maxwell–Garnett relation model. (a) Water phase fraction. (b) Oil phase fraction. (c) Air phase fraction. The dashed lines indicate a deviation of ±20.

TABLE V

AVERAGE RELATIVE ERROR FOR EVERY PHASE FRACTION USING THE RELATION MODELS FOR EACH FLOW PATTERN

Relation Model	*ARE* Water [%]	*ARE* Air [%]	*ARE* Oil [%]	*Flow Pattern*
Maxwell	12.99	13.38	22.48	All the experiments
	10.50	7.98	22.03	WChBoDo
	16.30	9.43	7.53	OPiBoDi
	11.55	16.36	28.36	WPiBoDo
Bruggeman	151.54	84.85	155.05	All the experiments
	108.98	16.46	28.67	WChBoDo
	209.02	76.09	86.29	OPiBoDi
	130.63	107.64	224.05	WPiBoDo
Parallel	36.76	71.34	82.29	All the experiments
	30.35	16.21	70.57	WChBoDo
	46.39	26.14	11.89	OPiBoDi
	32.33	107.87	114.71	WPiBoDo
Series	329.27	85.33	85.59	All the experiments
	188.64	14.83	90.67	WChBoDo
	543.57	99.05	97.81	OPiBoDi
	258.69	97.36	163.48	WPiBoDo

characteristics, such as relative permittivity, are very close to those of the air, which increases the difficulty of differentiating them. More research is needed to sort it out.

It is important to note that these results were obtained for different flow patterns. In theory, it would be possible to improve the relative errors, points spreading, and trends if a permittivity model more appropriate for each flow pattern were applied. However, this does not guarantee that a permittivity model that is the best for slug flow and the water phase is also the best for the same flow pattern and any other phase. Besides, that approach embodies complexities and complications in the technique that would end up compromising the effectiveness of its use, since it is not known, *a priori*, what the flow pattern is in practice. That said, the results presented are considered sufficient for the subsequent studies of three-phase flow through the wire-mesh sensor. Therefore, the Maxwell–Garnett model is adopted for the analysis of the data acquired by the wire-mesh sensor for all three-phase flow patterns.

The WMT system's measurement uncertainty for three/phase flow has not yet been calculated and is expected to be analyzed in future work. Until now, Tompkins *et al.* [42] made an uncertainty analysis for several gas–liquid flow patterns, settling that the WMS has a void-fraction measurement uncertainty of ±10.5%.

IV. CONCLUSION

In this article, we introduce a WMT technique to measure simultaneously the conductivity and permittivity of fluids in a typical oil-water-air three-phase flow, with a digital technique. The implemented technique to determine the complex permittivity of the fluids was based on measuring its real and imaginary parts using a digital IQ demodulator. The circuit was simplified, because the physical implementation of the analog multipliers or LPFs is no longer necessary, and it avoids transmitting an analog reference signal, reducing noise. Due to the very good synchronization, using a PLL, and the fact that the number of samples per cycle (N_S) is an integer, the computational workload is decreased significantly allowing a high rate of frames per second and the study of fleeting transient structures. It is the first time that this system is explained in the available literature, describing essential processing details.

The system was tested in a big vertical experimental setup and several flow patterns were visually observed, with both water and oil as the dominant liquid phase. The flow patterns had mixed phases, not separated or stratified, and also big interfacial structures such as Taylor bubbles.

The qualitative results are promising and suggest that the technique is a good option for three-phase flow tomography. The developed technique opens a great range of research possibilities, for example, new data to adjust or improve volumetric-fraction mathematical prediction models. Data as interfacial areas, bubble size classification, among others, can be easily obtained from the images. One of the advantages of the proposed technique is the relatively simple way of calibrating the system. The WMT has a high temporal resolution, which makes it feasible to apply it in the study of transient phenomena in multiphase flow. This system allows the real-time monitoring of extremely fast three-phase flow events, i.e., actual 3-D details about the Taylor bubbles and phases distributions can be visualized inside of the pipeline.

Also, quantitatively, the results are encouraging, having average relative errors for the volumetric phase fractions, compared with QCVs, of 12% for water, 13% for air, and 22% for oil. Future work will be focused on improving the relation models, quantitative results, and uncertainty analyses.

References

[1] B. Jia, J.-S. Tsau, and R. Barati, "A review of the current progress of CO_2 injection EOR and carbon storage in shale oil reservoirs," *Fuel*, vol. 236, pp. 404–427, Jan. 2019, doi: 10.1016/j.fuel.2018.08.103.

[2] S. Huang, B. Zhang, J. Lu, and D. Wang, "Study on flow pattern maps in hilly-terrain air–water–oil three-phase flows," *Exp. Thermal Fluid Sci.*, vol. 47, pp. 158–171, May 2013, doi: 10.1016/j.expthermflusci.2013.01.011.

[3] P. Hanafizadeh, A. Shahani, A. Ghanavati, and M. A. Akhavan-Behabadi, "Experimental investigation of air-water-oil three-phase flow patterns in inclined pipes," *Exp. Thermal Fluid Sci.*, vol. 84, pp. 286–298, Jun. 2017, doi: 10.1016/j.expthermflusci.2017.02.009.

[4] K. Gawas, *Studies in Low-Liquid Loading in Gas/Oil/Water Three Phase Flow in Horizontal and Near Horizontal Pipes*. Tulsa, OK, USA: Univ. Tulsa, 2013.

[5] S. Wang, H.-Q. Zhang, C. Sarica, and E. Pereyra, "Experimental study of high-viscosity oil/water/gas three-phase flow in horizontal and upward vertical pipes," *SPE Prod. Oper.*, vol. 28, no. 3, pp. 306–316, Jul. 2013, doi: 10.2118/163148-PA.

[6] X. Liu, H. Zhong, Y. Li, Z. Li, and Q. Wang, "Experimental study of flow patterns and pressure drops of heavy oil-water-gas vertical flow," *J. Hydrodyn. B*, vol. 26, no. 4, pp. 646–653, Sep. 2014, doi: 10.1016/S1001-6058(14)60071-8.

[7] B. Xie, D. Kong, L. Kong, W. Kong, and L. Li, "Analysis of vertical upward oil-gas-water three-phase flow based on multi-scale time irreversibility," *Flow Meas. Instrum.*, vol. 62, pp. 9–18, Aug. 2018, doi: 10.1016/j.flowmeasinst.2018.03.003.

[8] L. M. Al-Hadhrami, S. M. Shaahid, L. O. Tunde, and A. Al-Sarkhi, "Experimental study on the flow regimes and pressure gradients of air-oil-water three-phase flow in horizontal pipes," *Sci. World J.*, vol. 2014, Jan. 2014, Art. no. 810527, doi: 10.1155/2014/810527.

[9] G. Oddie, H. Shi, L. J. Durlofsky, K. Aziz, B. Pfeffer, and J. A. Holmes, "Experimental study of two and three phase flows in large diameter inclined pipes," *Int. J. Multiph. Flow*, vol. 29, no. 4, pp. 527–558, Apr. 2003, doi: 10.1016/S0301-9322(03)00015-6.

[10] C. Zhao, G. Wu, H. Zhang, and Y. Li, "Measurement of water-to-liquid ratio of oil-water-gas three-phase flow using microwave time series method," *Meas. J. Int. Meas. Ed.*, vol. 140, pp. 511–517, Jul. 2019, doi: 10.1016/j.measurement.2019.03.054.

[11] M. W. Yaqub, R. Marappagounder, R. Rusli, D. M. R. Prasad, and R. Pendyala, "Review on gas–liquid–liquid three–phase flow patterns, pressure drop, and liquid holdup in pipelines," *Chem. Eng. Res. Des.*, vol. 159, pp. 505–528, Jul. 2020, doi: 10.1016/j.cherd.2020.04.029.

[12] L. Edwards, D. Dhanpat, and D. P. Chakrabarti, "Hydrodynamics of three phase flow in upstream pipes," *Cogent Eng.*, vol. 5, no. 1, pp. 1–28, Jan. 2018, doi: 10.1080/23311916.2018.1433983.

[13] E. N. dos Santos, T. P. Vendruscolo, R. E. M. Morales, E. Schleicher, U. Hampel, and M. J. Da Silva, "Dual-modality wire-mesh sensor for the visualization of three-phase flows," *Meas. Sci. Technol.*, vol. 26, no. 10, Oct. 2015, Art. no. 105302, doi: 10.1088/0957-0233/26/10/105302.

[14] F. D. A. Dias *et al.*, "New algorithm to discriminate phase distribution of gas-oil-water pipe flow with dual-modality wire-mesh sensor," *IEEE Access*, vol. 8, pp. 125163–125178, 2020, doi: 10.1109/ACCESS.2020.3007678.

[15] L. Zhai, Y. Wang, J. Yang, and N. Jin, "A three-phase flow visualization method using wire-mesh sensor based on continuous phase conductance compensation," in *Proc. IEEE Int. Instrum. Meas. Technol. Conf. (IMTC)*, May 2021, pp. 1–6, doi: 10.1109/I2MTC50364.2021.9459918.

[16] G. Bochio, M. M. H. Cely, A. F. A. Teixeira, and O. M. H. Rodriguez, "Experimental and numerical study of stratified viscous oil–water flow," *AIChE J.*, vol. 67, pp. 1–15, Feb. 2021, doi: 10.1002/aic.17239.

[17] J. L. Kickhofel, R. Zboray, M. Damsohn, A. Kaestner, E. H. Lehmann, and H.-M. Prasser, "Cold neutron tomography of annular coolant flow in a double subchannel model of a boiling water reactor," *Nucl. Instrum. Methods Phys. Res. A, Accel. Spectrom. Detect. Assoc. Equip.*, vol. 651, no. 1, pp. 297–304, Sep. 2011, doi: 10.1016/j.nima.2011.01.062.

[18] Z. Wu, H. McCann, L. E. Davis, J. Hu, A. Fontes, and C. G. Xie, "Microwave-tomographic system for oil- and gas-multiphase-flow imaging," *Meas. Sci. Technol.*, vol. 20, no. 10, Oct. 2009, Art. no. 104026, doi: 10.1088/0957-0233/20/10/104026.

[19] E. Schleicher, M. J. da Silva, S. Thiele, A. Li, E. Wollrab, and U. Hampel, "Design of an optical tomograph for the investigation of single- and two-phase pipe flows," *Meas. Sci. Technol.*, vol. 19, no. 9, Sep. 2008, Art. no. 094006, doi: 10.1088/0957-0233/19/9/094006.

[20] T. Frøystein, H. Kvandal, and H. Aakre, "Dual energy gamma tomography system for high pressure multiphase flow," *Flow Meas. Instrum.*, vol. 16, nos. 2–3, pp. 99–112, Apr. 2005, doi: 10.1016/j.flowmeasinst.2005.02.005.

[21] S. Schug and W. Arlt, "Imaging of fluid dynamics in a structured packing using X-ray computed tomography," *Chem. Eng. Technol.*, vol. 39, no. 8, pp. 1561–1569, Aug. 2016, doi: 10.1002/ceat.201600278.

[22] M. Appel, J. J. Freeman, and D. Pusiol, "Robust multi-phase flow measurement using magnetic resonance technology," in *Proc. SPE Middle East Oil Gas Show Conf.*, Manama, Bahrain, Sep. 2011, doi: 10.2118/141465-MS.

[23] A. Alfareh, M. H. F. Rahiman, M. T. M. Talib, J. Pusppanathan, and J. Jamaludin, "Simulation of invasive ultrasonic tomography for three phase mixture," *J. Telecommun. Electron. Comput. Eng.*, vol. 10, nos. 1–13, pp. 129–133, 2018.

[24] Y. Li *et al.*, "Gas/oil/water flow measurement by electrical capacitance tomography," *Meas. Sci. Technol.*, vol. 24, no. 7, Jul. 2013, Art. no. 074001, doi: 10.1088/0957-0233/24/7/074001.

[25] B. Wang, Z. Gui, W. Tan, Z. Huang, H. Ji, and H. Li, "A new dual-modality ECT/ERT technique based on C4D principle," in *Proc. IEEE Int. Instrum. Meas. Technol. Conf. (IMTC)*, May 2015, pp. 2061–2065, doi: 10.1109/I2MTC.2015.7151600.

[26] J. Sun and W. Yang, "A dual-modality electrical tomography sensor for measurement of gas-oil-water stratified flows," *Measurement*, vol. 66, no. 5, pp. 150–160, Apr. 2015, doi: 10.1016/j.measurement.2015.01.032.

[27] Q. Wang *et al.*, "Capability of dual-modality electrical tomography for gas-oil-water three-phase pipeline flow visualisation," *Flow Meas. Instrum.*, vol. 62, pp. 152–166, Aug. 2018, doi: 10.1016/j.flowmeasinst.2018.02.007.

[28] F. Hernandez-Alvarado, S. Kleinbart, D. V. Kalaga, S. Banerjee, J. B. Joshi, and M. Kawaji, "Comparison of void fraction measurements using different techniques in two-phase flow bubble column reactors," *Int. J. Multiphase Flow*, vol. 102, pp. 119–129, May 2018, doi: 10.1016/j.ijmultiphaseflow.2018.02.002.

[29] A. J. Dave, A. Manera, M. Beyer, D. Lucas, and H.-M. Prasser, "Uncertainty analysis of an interfacial area reconstruction algorithm and its application to two group interfacial area transport equation validation," *Nucl. Eng. Des.*, vol. 310, pp. 620–637, Dec. 2016, doi: 10.1016/j.nucengdes.2016.10.038.

[30] I. D. Johnson, "Method and apparatus for measuring water in crude oil," U.S. Patent 4 664 263, Feb. 17, 1987.

[31] H.-M. Prasser, A. Böttger, and J. Zschau, "A new electrode-mesh tomograph for gas–liquid flows," *Flow Meas. Instrum.*, vol. 9, no. 2, pp. 111–119, Jun. 1998.

[32] M. J. Da Silva, E. Schleicher, and U. Hampel, "Capacitance wire-mesh sensor for fast measurement of phase fraction distributions," *Meas. Sci. Technol.*, vol. 18, no. 7, pp. 2245–2251, Jul. 2007, doi: 10.1088/0957-0233/18/7/059.

[33] H. F. V. Peña and O. M. H. Rodriguez, "Applications of wire-mesh sensors in multiphase flows," *Flow Meas. Instrum.*, vol. 45, pp. 255–273, Oct. 2015, doi: 10.1016/j.flowmeasinst.2015.06.024.

[34] M. J. da Silva, "Impedance sensors for fast multiphase flow measurement and imaging," Ph.D. dissertation, Dept. Elect. Comput. Eng., Dresden, Germany, TUDpress, 2008.

[35] E. N. dos Santos, M. J. da Silva, R. E. M. Morales, S. Reinecke, E. Schleicher, and U. Hampel, "Dual-modality impedance wire-mesh sensor for investigation of multiphase flows," in *Proc. IEEE Int. Conf. Imag. Syst. Techn. (IST)*, Oct. 2014, pp. 316–319, doi: 10.1109/IST.2014.6958496.

[36] E. N. dos Santos, "Development and application of wire-mesh sensors for high-speed multiphase flow imaging," M.S. thesis, Dept. Elect. Eng., Federal Univ. Technol. Paraná, Curitiba, Brazil, 2015.

[37] H.-M. Prasser and R. Häfeli, "Signal response of wire-mesh sensors to an idealized bubbly flow," *Nucl. Eng. Des.*, vol. 336, pp. 3–14, Sep. 2018, doi: 10.1016/j.nucengdes.2017.04.016.

[38] H. Zhang, Y. Xiao, and H. Gu, "Numerical investigations of the accuracy of conductivity wire-mesh sensors," *Nucl. Eng. Des.*, vol. 345, pp. 148–156, Apr. 2019, doi: 10.1016/j.nucengdes.2019.02.014.

[39] M. J. Da Silva, F. Bruckner, E. Schleicher, and U. Hampel, "High-speed complex admittance/permittivity needle probe for investigation of multiphase flows," in *Proc. IEEE Instrum. Meas. Technol. Conf.*, Apr. 2006, pp. 1937–1941, doi: 10.1109/IMTC.2006.328315.

[40] A. Sihvola, *Electromagnetic Mixing Formulas and Applications*. London, U.K.: The Institution of Engineering and Technology, 1999.

[41] I. H. Rodriguez, H. F. V. Peña, A. B. Riaño, R. A. W. M. Henkes, and O. M. H. Rodriguez, "Experiments with a wire-mesh sensor for stratified and dispersed oil-brine pipe flow," *Int. J. Multiphase Flow*, vol. 70, pp. 113–125, Apr. 2015, doi: 10.1016/j.ijmultiphaseflow.2014.11.011.

[42] C. Tompkins, H.-M. Prasser, and M. Corradini, "Wire-mesh sensors: A review of methods and uncertainty in multiphase flows relative to other measurement techniques," *Nucl. Eng. Des.*, vol. 337, pp. 205–220, Oct. 2018, doi: 10.1016/j.nucengdes.2018.06.005.

[43] D. M. Rocha, C. H. M. de Carvalho, V. Estevam, and O. M. H. Rodriguez, "Effects of water and gas injection and viscosity on volumetric fraction, pressure gradient and phase inversion in upward-vertical three-phase pipe flow," *J. Petroleum Sci. Eng.*, vol. 157, pp. 519–529, Aug. 2017, doi: 10.1016/j.petrol.2017.07.055.

Hugo Fernando Velasco-Peña (Senior Member, IEEE) received the B.S. degree in electronics engineering from the Francisco José de Caldas University, Bogotá, Colombia, in 2003, the M.Sc. degree in industrial automation from the National University of Colombia, Bogotá, in 2010, and the Ph.D. degree in mechanical engineering from the University of São Paulo, São Paulo, Brazil, in 2015.

He is currently an Associate Professor with the Universidad de La Salle, Bogotá. His experience is related with industrial instrumentation, smart sensors, and signal and image processing.

Adriana Bonilla-Riaño received the B.S. degree in electronics engineering from the Francisco José de Caldas University, Bogotá, Colombia, in 2003, the M.Sc. degree in electronics engineering from Pontifical Javeriana University, Bogotá, in 2010, and the Ph.D. degree in petroleum sciences and engineering from the University of Campinas in Brazil, Campinas, Brazil, in 2015.

She had presented her research results in different international conferences and high-impact journals. Her research interests include signal and image processing and electronic instrumentation.

Carlos Marlon Santos received the B.S. degree in mechanical engineering from the Federal University of Bahia, Salvador, Brazil, in 2002, the M.Sc. degree in mechanical engineering from the Federal University of Paraiba, João Pessoa, Brazil, in 2005, and the Ph.D. degree in mechanical engineering from the University of São Paulo, São Paulo, Brazil, in 2020.

His research interest includes multiphase flow.

Oscar M. H. Rodriguez received the B.S. degree in mechanical engineering from the Federal University of Uberlandia, Brazil, in 1996, and the M.Sc. and Ph.D. degrees in mechanical engineering from the State University of Campinas, Campinas, Brazil, 1998 and 2002, respectively.

He was a Research Fellow at the Delft University of Technology, Delft, The Netherlands, and the University of Nottingham, Nottingham, U.K. He is currently an Associate Professor with the University of São Paulo (USP), São Paulo, Brazil, where he is also the Coordinator of the Multiphase Flow Research Center. He has authored more than 150 complete scientific articles. His research interests include multiphase flow, hydrodynamic instability, electrical-impedance instrumentation, and energy industry.

Dr. Rodriguez is a member of the Management Board of the European Research Community on Flow, Turbulence and Combustion (ERCOFTAC). He was a recipient of the EMBRAER Best Doctoral Thesis and PETROBRAS Technology Awards. He was the Chairperson for the 10th International Conference on Multiphase Flow—ICMF 2019.